Observation of multiple off-site corner states induced by next-nearest-neighbor coupling in a sonic crystal

Wei Xiong,[1] Shuochen Wang,[1] Zhiwang Zhang,[1,*] Haixiao Zhang,[2] Ying Cheng,[1,3,†] and Xiaojun Liu[1,3,‡]

[1]*Department of Physics, Collaborative Innovation Center of Advanced Microstructures, Nanjing University, Nanjing 210093, China*

[2]*School of Electrical and Information Engineering, Changzhou Institute of Technology, Changzhou 213032, China*

[3]*State Key Laboratory of Acoustics, Institute of Acoustics, Chinese Academy of Sciences, Beijing 100190, China*

(Received 13 September 2023; revised 28 November 2023; accepted 8 December 2023; published 10 January 2024)

The unexpected connections between classical wave phenomena and higher-order topological phases have attracted the interest of researchers across various fields. Although attaining lower-dimensional localized states, such as corner states, has been a common achievement in the realm of sonic crystals, a notable limitation arises where wave energy primarily localizes at the outermost site with the degenerate eigenfrequencies, thereby restricting further applications in acoustics. In this paper, we address this limitation by introducing previously overlooked extra next-nearest-neighbor interactions into the system. Remarkably, the inclusion of these extra nonlocal interactions generates an array of unconventional corner-localized states, each with distinct off-site localization positions. Experimental validation of these theoretical predictions is meticulously conducted using fabricated sonic crystals. Notably, in contrast to natural crystals, the advantageous characteristics of artificial crystals provide a promising platform for probing the effect of long-range interactions in topological phases and materials, which is facilitated by distance-independent coupling strengths. Our findings not only expand the boundaries of sound confinement but also provide momentum for exploring long-range interactions in the field of artificial crystals.

DOI: 10.1103/PhysRevB.109.024305

I. INTRODUCTION

Topological insulators (TIs) [1,2] have attracted increasing attention in the field of condensed matter physics due to their unique conducting states on edges or surfaces that are protected against scattering. The principle of bulk-boundary correspondence [1] states that nontrivial TIs of dimensionality d possess lower-dimensional boundary states of dimensionality $(d-1)$. More recently, a new class of topological insulators called higher-order topological insulators [3–8] (HOTIs) has emerged. HOTIs are characterized by higher bulk multipole moments and lower-dimensional boundary signatures that expand the traditional bulk-boundary correspondence. Specifically, second-order TIs in two dimensions (2D) exhibit zero-dimensional (0D) corner states, while in three dimensions (3D), they give rise to one-dimensional (1D) hinge states. In various 2D systems with different symmetries, such as the kagome lattice with C_3 symmetry, the Su-Schrieffer-Heeger (SSH) lattice with C_4 symmetry, and the honeycomb lattice with C_6 symmetry, the second-order TIs have been successfully realized [4,8,9]. Moreover, HOTIs have been extensively engineered using artificial materials in various fields, including photonics [10–16], electric circuits [17–19], mechanics [20–22], and acoustics [23–34].

Acoustic systems have gained substantial traction as a versatile platform for realizing a spectrum of HOTIs due to their exceptional macroscopic controllability and tunability. Moreover, this platform has facilitated the exploration of extended concepts such as higher-order semimetals [35–37], Floquet HOTIs [38], and non-Hermitian HOTIs [27]. On the other hand, recent intriguing topological phases have emerged in 1D sonic SSH lattices featuring significant long-range interactions [39]: a challenging achievement within solid-state systems where electron coupling strength is distance dependent. This development naturally prompts the question of how long-range interactions influence the HOTIs. Moreover, despite the significant application potential of the strong localizations having been demonstrated in the aforementioned acoustic HOTIs, certain limitations persist. Specifically, the acoustic energy remains confined solely to the outermost *in situ* units, and the eigenfrequencies are degenerate and pinned at one specific value. These limitations hinder further applications such as sound demultiplexing based on the distinct positions and frequency components.

To address these issues, we present in this paper a solution in which an acoustic HOTI featuring robust next-nearest-neighbor (NNN) coupling [13,39–41] is established. Furthermore, we provide experimental evidence of the remarkable off-site multipolar corner states, which exhibit diverse spatial and frequency properties. Particularly, these spatial properties involve distinct spatial locations and phase profiles. To illustrate this approach, we focus on the kagome lattice as a representative example due to its well-known

*zhangzhiwang@nju.edu.cn
†chengying@nju.edu.cn
‡liuxiaojun@nju.edu.cn

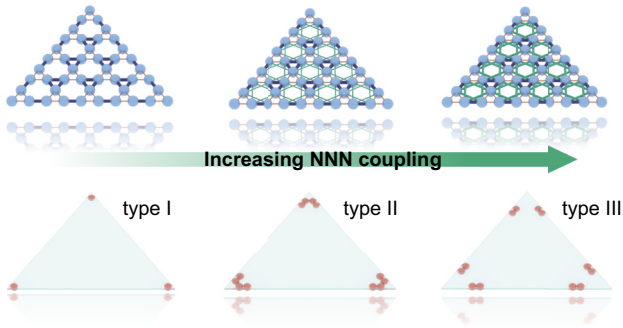

FIG. 1. Schematic illustrating the successive appearance of type II and type III corner states in HOTIs as the NNN coupling strength increases.

ability to host higher-order topological phases. Nevertheless, it is important to note that this approach is universally applicable and can be extended to other HOTIs characterized by different symmetries. We progressively increase the NNN coupling strength in the tight-binding model (TBM) of the kagome lattice to determine the critical strength required for separating type II and type III corner states from the edge states (see Fig. 1). Subsequently, we employ a coupled-cavity model to construct the corresponding acoustic kagome lattice. Supplementary connecting tubes are introduced to achieve appropriate NNN interactions, effectively interlinking the second-nearest-neighbor resonators. The higher-order topological characteristics manifest through quantized bulk polarizations. Our experimental exploration verifies the presence of these captivating corner states by meticulously scrutinizing acoustic responses and the associated pressure fields. Beyond the conventional zero-energy corner states (ZECSs) localized in the *in situ* cornermost cavities, we discern four additional off-site corner states exhibiting distinct phase distributions and localization sites. This underscores the exceptional flexibility and versatility of our design in terms of acoustic manipulation and localization, especially when contrasted with scenarios devoid of near-neighbor coupling or characterized by weak tight-neighbor coupling.

II. RESULTS

A. Tight-binding model

We begin by considering the TBM for the kagome lattice where the additional long-range coupling terms are incorporated to explore the emergence of exotic off-site corner states, as illustrated in Fig. 2(a). Each unit cell consists of three sites labeled as sites 1–3. The nearest-neighbor (NN) couplings are characterized by brown lines and dark blue lines, which correspond to the intracell (t_0) and intercell (t_1) local interactions, respectively. Then we specifically focus on the long-range interactions that are solely influenced by the NNN coupling (t_2), represented by green lines. The finite triangular kagome lattice comprises $(N+1)\times N/2$ unit cells, where N represents the number of unit cells on each side. When $t_2 = 0$ and $t_1 > t_0$, the kagome model exhibits nontrivial higher-order band topology, leading to the presence of ZECSs localized at the cornermost sites, which has been extensively studied [13,24,25].

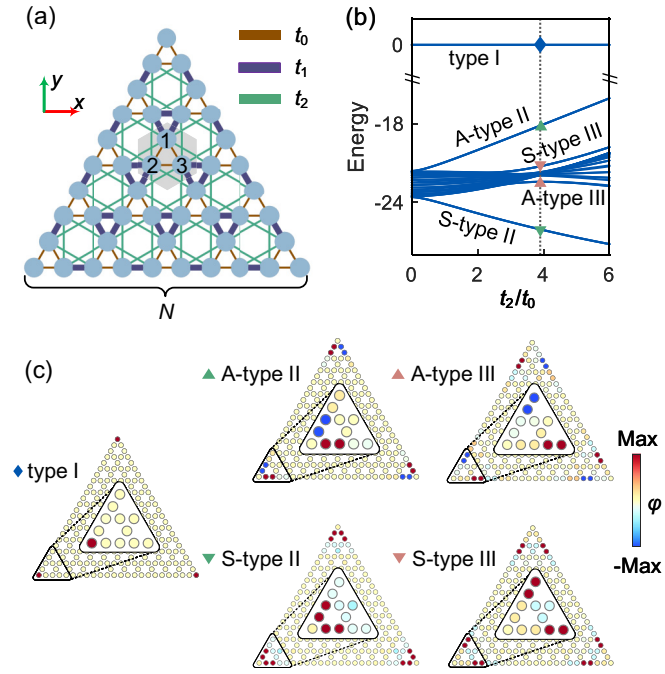

FIG. 2. Tight-binding model. (a) Finite-sized kagome lattice with NNN coupling, consisting of $(N+1)\times N/2$ unit cells. Brown, dark blue, and green lines denote the intracell coupling t_0, intercell coupling t_1, and NNN coupling t_2, respectively. (b) Energy spectrum with the fixed ratio of $t_1/t_0 = 22.6$ but varying t_2. (c) Wave functions φ of different corner states: type I, antisymmetric type II (A-type II), symmetric type II (S-type II), antisymmetric type III (A-type III), and symmetric type III (S-type II) corner states. The dotted line in (b) represents $t_2/t_0 = 3.9$.

Building upon this phase, we investigate the case of $N = 12$ and analyze the energy spectrum as a function of NNN coupling strength while maintaining $t_1/t_0 = 22.6$ constant. We focus on the energy spectrum within the band gap, as depicted in Fig. 2(b). With an increasing strength of NNN coupling t_2/t_0, two pairs of distinct states sequentially deviate from the edge states, exhibiting energies different from those of the ZECSs (referred to as type I corner states). In the kagome lattice with the extra NNN coupling, there exist type III corner states at most capable of emerging from the edge states (see Supplemental Material Note I for details [42]). To confirm the corner localization of these emerging states, we present the wave functions φ of the eigenstates in Fig. 2(c), highlighting a specific value of t_2/t_0 indicated by the vertical dotted line in Fig. 2(b). The additional type II and type III corner states exhibit two notable characteristics that distinguish them from the conventional type I ZECSs. Firstly, they are localized near the corners, although not precisely at the cornermost site. More specifically, the highest field values of the type II (type III) corner states occur at the second and third (fourth and fifth) sites adjacent to the cornermost site. Secondly, both type II and type III corner states exhibit two distinct sets of eigenvalues, displaying symmetric (S) or antisymmetric (A) field profiles with respect to the angle bisector of each corner. The presence of these off-site corner-localized states with tunable localization points and diverse phase profiles offers alternative possibilities for manipulating wave behavior using

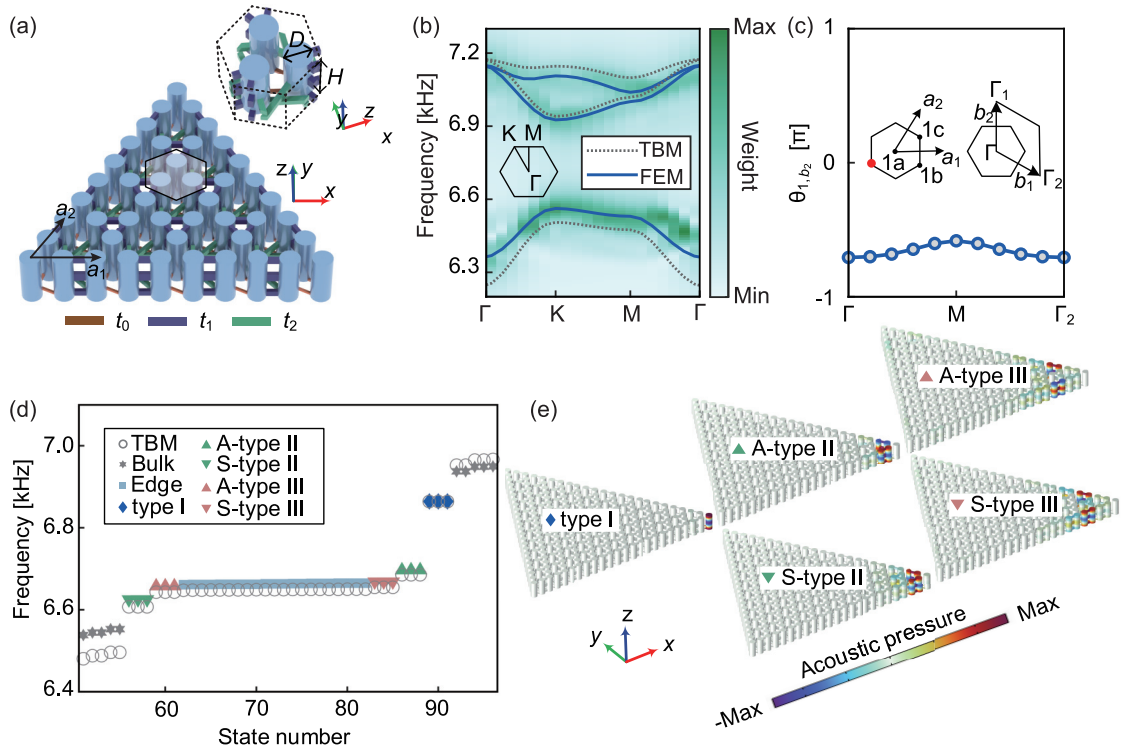

FIG. 3. Acoustic cavity-tube model. (a) Schematic of a triangle-shaped acoustic kagome lattice, which consists of identical cavity resonators connected by three different types of coupling tubes. The lattice constant is $a = 6.04$ cm. Inset: enlarged side view of the metamolecule, with different colors used to distinguish the various coupling tubes. (b) Bulk band structure of the acoustic cavity-tube system (blue solid curve) along high-symmetry directions, compared with the TBM (gray dotted curve) and measured bulk band (background color map). (c) Wilson loop for the first band below the band gap concerned based on the acoustic kagome lattice with NNN coupling. The insets show the location of real-space Wannier centers (indicated by the red dot in the left inset) in the unit cell and the deformed rhombic Brillouin zone in the numerical calculation of bulk polarization. The black points 1*a*, 1*b*, and 1*c* are the maximal Wyckoff positions. (d) Corresponding corner spectra calculated for finite-sized cavity-tube samples and the TBM. (e) Spatial distributions of the acoustic pressure for type I, type II, and type III corner states from eigenstate calculations.

HOTIs when applied to artificial crystals. Note that these phenomena are not reliant on specific crystal symmetry; thus similar outcomes can be obtained when applying long-range interactions to other HOTIs with different symmetries. In Supplemental Material Notes II–IV [42] (see also Refs. [43,44] therein), for example, we have studied the 2D SSH lattice in a similar way.

B. Acoustic kagome lattice with NNN coupling

To emulate the kagome TBM with NNN coupling, we employ an acoustic cavity-tube model [45]. The unit cell of the acoustic kagome lattice, as shown in the inset at the top right of Fig. 3(a), has three identical cylindrical cavity resonators with dimensions of $H = 50$ mm and $D = 20$ mm, arranged with a lattice constant of $a = 60.4$ mm. The second-order resonant mode (6864 Hz) of each resonator serves as the on-site orbital. To simulate the NN couplings (t_0, t_1) and NNN coupling (t_2), colored connecting tubes are introduced between the corresponding resonators. Supplemental Material Note V [42] provides additional details regarding the system's geometry. In comparison to the previous designs of acoustic kagome lattices [24,25], our design distinguishes itself by incorporating long-range interactions via additional tubes that connect the resonators of the next-nearest neighbors, thus introducing extra nonlocal intercell coupling. While it is also possible for acoustic cavity-waveguide systems to have nonzero long-range couplings, these couplings are typically determined by the distance between the cavities and cannot be tunably controlled. Concretely, the strength of the NNN coupling will not be greater than the NN couplings. This limitation restricts the emergence of type III and subsequent rich type *N* corner states. Our proposed acoustic cavity-tube system overcomes this restriction by allowing the coupling strength to be quantitatively and individually tailored through the geometry parameters of the coupling tubes, specifically the cross-sectional area and the positions of their two ends. Furthermore, our design can be accurately described by a TBM, which is crucial for this work as we need specific NNN coupling to observe type II and type III corner states [see Figs. 2(b) and 2(c)].

Guided by the theoretical predictions based on the TBM shown in Fig. 2(b), we optimize the geometry parameters of the coupling tubes to achieve the desired coupling strength and preserve the chiral symmetry of our acoustic model [46,47]. The intracell (intercell) couplings, $t_0 = -9.9$ Hz ($t_1 = -222.6$ Hz), are realized using brown (dark blue) tubes, and the NNN coupling, $t_2 = -38.7$ Hz, is

realized using the longer green tubes. To confirm the consistency between the acoustic kagome lattice and the TBM, we independently computed the bulk band structures of both models, as shown in Fig. 3(b). The bulk band structure of the acoustic model is obtained using the finite-element method, while the TBM's band structure is directly derived from the Bloch Hamiltonian. We also measured the bulk band in experiment, which is represented by the color scale in Fig. 3(b). The experimental results closely match the simulated and theoretical band structures. The explicit Hamiltonian in momentum space can be described by the following equation:

$$\mathcal{H}(\boldsymbol{k}) = \begin{bmatrix} 0 & t_0 + t_1\bar{\chi}_{\boldsymbol{k}}^{(2)} & t_0 + t_1\chi_{\boldsymbol{k}}^{(3)} \\ t_0 + t_1\chi_{\boldsymbol{k}}^{(2)} & 0 & t_0 + t_1\chi_{\boldsymbol{k}}^{(1)} \\ t_0 + t_1\bar{\chi}_{\boldsymbol{k}}^{(3)} & t_0 + t_1\bar{\chi}_{\boldsymbol{k}}^{(1)} & 0 \end{bmatrix} + t_2 \begin{bmatrix} 0 & \bar{\chi}_{\boldsymbol{k}}^{(1)} + \chi_{\boldsymbol{k}}^{(3)} & \bar{\chi}_{\boldsymbol{k}}^{(2)} + \chi_{\boldsymbol{k}}^{(1)} \\ \bar{\chi}_{\boldsymbol{k}}^{(3)} + \chi_{\boldsymbol{k}}^{(1)} & 0 & \chi_{\boldsymbol{k}}^{(3)} + \chi_{\boldsymbol{k}}^{(2)} \\ \bar{\chi}_{\boldsymbol{k}}^{(1)} + \chi_{\boldsymbol{k}}^{(2)} & \bar{\chi}_{\boldsymbol{k}}^{(3)} + \bar{\chi}_{\boldsymbol{k}}^{(2)} & 0 \end{bmatrix}, \tag{1}$$

where $\chi_{\boldsymbol{k}}^{(i)} = e^{-i\boldsymbol{k}\cdot\boldsymbol{a}_i}$ for $i = 1, 2, 3$, $\boldsymbol{a}_1 = a(1, 0), \boldsymbol{a}_2 = a(\frac{1}{2}, \frac{\sqrt{3}}{2})$, and $\boldsymbol{a}_3 = a(\frac{1}{2}, -\frac{\sqrt{3}}{2})$. Despite the inclusion of an additional coupling term, the C_3 symmetry of the Hamiltonian is preserved. In Supplemental Material Note VI [42], we further discuss the situation under the broken C_3 symmetry. A band gap exists between the first two bands. In the absence of NNN coupling ($t_2 = 0$), the system exhibits higher-order topological insulator phases for $0 < t_0/t_1 < 1$.

We demonstrate that the bulk polarization can be utilized to characterize the topological phase, which is defined as $\mathbf{P} = (p_1\boldsymbol{a}_1 + p_2\boldsymbol{a}_2)$ in terms of the lattice vectors $\boldsymbol{a}_1$ and $\boldsymbol{a}_2$ in real space [4]. The polarization components p_1 and p_2 are calculated using the Wilson-loop approach as [48]

$$p_\alpha = \frac{1}{2\pi}\int_L \mathrm{d}\theta_{\alpha,b_\beta}, \quad \alpha = 1, 2, \quad \beta = 1, 2, \tag{2}$$

where L denotes the projection length of the Brillouin zone (BZ) along the b_α direction and θ_{α,b_β} is the calculated Berry phase along loop b_β for a fixed b_α. The reciprocal lattice vectors $\boldsymbol{b}_1 = \frac{2\pi}{a}(1, \frac{-1}{\sqrt{3}})$ and $\boldsymbol{b}_2 = \frac{2\pi}{a}(0, \frac{2}{\sqrt{3}})$ are related by the C_3 symmetry in the BZ, as illustrated in the right inset of Fig. 3(c). Utilizing these vectors, we can derive the calculation result of the acoustic coupled-cavity model of θ_{1,b_2} as a function of $\boldsymbol{b}_2$, which is swept from Γ to Γ_2. Combining the restriction imposed by the C_3 symmetry and the calculation results, we derive a nonzero polarization component as $p_1 = p_2 = -\frac{1}{3}$, which indicates the topologically nontrivial phase. As shown in the left inset of Fig. 3(c), the related Wannier centers are located at the maximal Wyckoff position 1*b*. Since the Wannier center is mismatched with the unit-cell center, this Wannier configuration confirms the obstructed atomic insulator nature of our structure, leading to the existence of the topological edge states and the zero-energy corner states. On this basis, the emergence of the type II and type III corner states is induced by the coupling between topological edge states (see Supplemental Material Note I for details [42]).

The eigenspectrum shown in Fig. 3(d) is the result of simulating a triangle-shaped finite acoustic model with $N = 12$ (colored polygons), and it demonstrates good agreement with the TBM results (gray circles). As anticipated, the eigenspectrum displays various states, including edge states (light blue squares) and type I (blue diamonds), type II (green triangles), and type III (red triangles) corner states. Type II and type III corner states demonstrate two distinct sets of states above and below the edge states, whereas type I corner states are pinned to zero energy. Similar to the type I corner states, each set of type II and type III corner states is triple degenerate. The field profiles shown in Fig. 3(e) allow us to distinguish between the two sets of type II and type III corner states. In the case of type II corner states, the set with a higher frequency exhibits an antisymmetric acoustic pressure field, while the other set displays a symmetric acoustic pressure field, which are referred to as A-type II and S-type II, respectively. The situation is reversed for the type III corner states, as evident from the spatial characteristics of the field profiles. In contrast to the type I corner states, which are localized on the cornermost cavity, the acoustic pressure of type II corner states is highly concentrated at the next two cavities adjacent to the corner cavity. On the other hand, the type III corner states are localized at the fourth and fifth cavities. These characteristics align with our expectations discussed in the previous section.

C. Observation of multiple off-site localized corner states

In experiments, we 3D-print the sample with photosensitive resins, as depicted in Fig. 4(a). The fabricated acoustic kagome lattice consists of 12 unit cells along each side and a total of 234 resonators. During detections, a pump-probe scheme is employed. There are two holes on the opposite sites of one cavity for inserting the acoustic source (loudspeaker) and detector (microphone), denoted as red and blue stars in the inset of Fig. 4(a), respectively (see Supplemental Material Note VII [42] for details). This sonic crystal is expected to support five different localized corner states, namely type I, A-type II, S-type II, S-type III, and A-type III ones. To fully investigate and analyze these different states, various detection configurations need to be considered. In Fig. 4(a), the resonators used for exciting and measuring signals in each configuration are denoted by different Arabic numerals (1–9), each associated with colored dots. Besides, through exciting sound waves at site 8, bulk states are detected at site 9 to reveal the band gap. To measure the response spectra of the edge state, a loudspeaker is placed at resonator 6 to excite sound waves, and the signals are detected at resonator 7. Corresponding measured intensity spectra of all these localized states are presented in Fig. 4(b). Arrows on the frequency axis denote the frequency peaks of the different localized corner states. For type I corner states, the resonator at site 1 is used for excitation and measurement, showing a single peak at a frequency of 6863 Hz. Due to the close frequency proximity of the symmetric and antisymmetric states for both type II and type III corner states, we excite two resonators simultaneously with two sources carrying different phases to overcome this issue. For example, to measure A-type II corner states, two antiphase sources (0 and π) were placed at site 2 and site 3. As expected, a single peak (6686 Hz) is measured at site 2 with the spectrum plotted in Fig. 4(b). In contrast, when in-phase sources are placed at the same sites, a

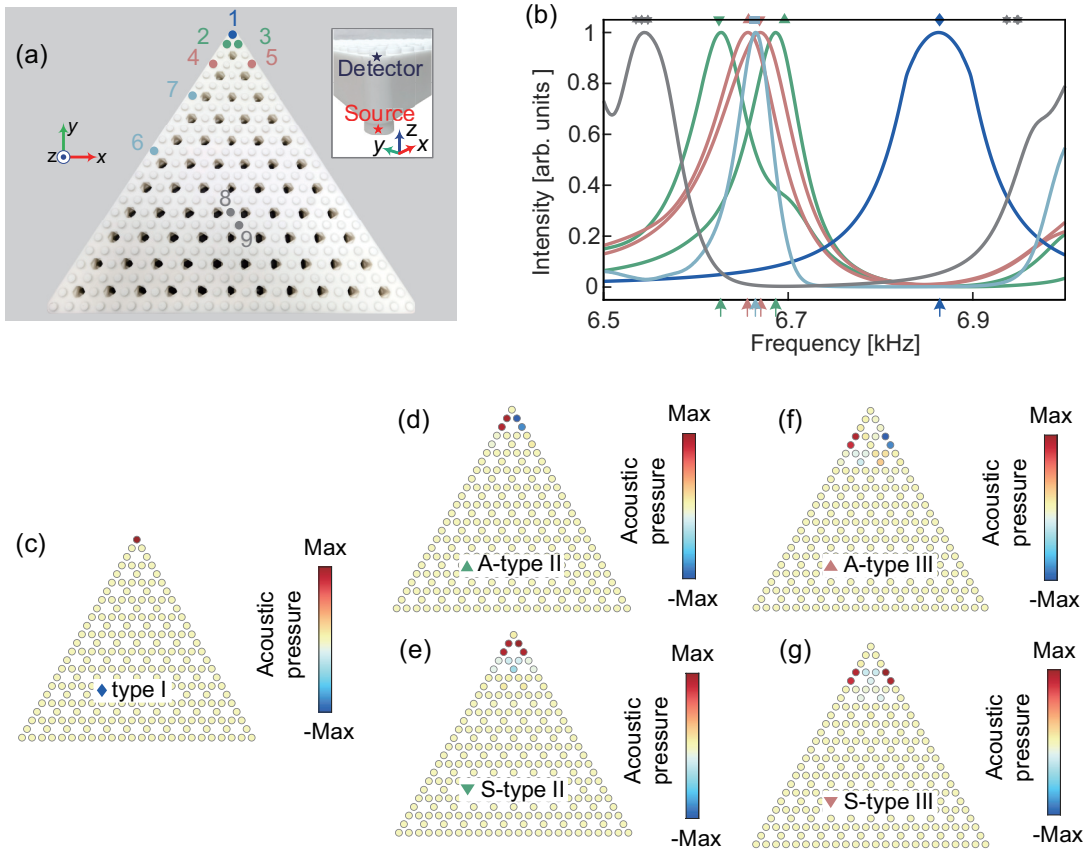

FIG. 4. (a) Top view of the 3D-printed acoustic kagome lattice. Inset: enlarged picture of the sample, in which the red and blue stars denote the acoustic source and detector, respectively. The excitation and detection resonators are marked by colored dots and labeled by Arabic numerals 1–9. (b) Measured spectra of the normalized intensity for the type I corner states (blue curve), type II corner states (green curves), type III corner states (red curves), edge states (light blue curve), and bulk states (gray curve). Peak frequencies are denoted by colored arrows at the bottom of the panel. Associated eigenfrequencies are denoted by symbols at the top of the panel. [(c)–(g)] Corresponding acoustic pressure profiles obtained from experimental measurements.

prominent peak with a lower frequency (6628 Hz) is obtained. The remaining two states are detected using the same strategy, with the sources placed at site 4 and site 5 instead. Two distinguishable signal peaks (6656 and 6670 Hz) are observed. All these measurements show excellent agreement with the corresponding simulated eigenfrequencies as denoted by the symbols shown at the top of Fig. 4(b).

In order to further validate the presence of distinctive topological localized states, we conduct measurements of the pressure field distributions at the peak frequencies of each spectrum. We compare the results for the four off-site localized corner states with those of the *in situ* corner states, as shown in Figs. 4(c)–4(g). In Fig. 4(c), the measured acoustic pressures of type I corner states are primarily concentrated at the corners, which is a characteristic feature of conventional HOTIs. However, for type II and type III corner states, the acoustic pressures are localized around the corners instead of being limited to the *in situ* cornermost resonator, as illustrated in Figs. 4(d)–4(g). These figures directly illustrate the unique properties of these states, exhibiting symmetric and antisymmetric behaviors with respect to the angle bisector, respectively. All these experimental measurements provide compelling evidence of the good agreement between our experimental observations and the numerical results presented in Fig. 3(e). We demonstrate that our proposed acoustic kagome lattice can also function as an efficient topological rainbow trapping device [49,50], capable of guiding and capturing acoustic waves with various frequencies accurately. This feature holds significant potential for applications in energy harvesting, demultiplexing, and wave filtering. Additionally, the presence of localization positions related to off-site corner states allows for capturing acoustic waves with symmetric and antisymmetric field distributions. This unique phase property of mode-division-multiplexing rainbow trapping scales the capacity of a single-wavelength component carrier by the number of modes, thereby creating fresh opportunities for enhancing the integration density in acoustic functional devices.

III. CONCLUSIONS

In conclusion, we have successfully demonstrated the existence of the multiple off-site corner states in acoustic HOTIs. By introducing long-range interactions through connectivity between NNN acoustic resonators, we have observed the emergence of the type II and type III corner states. These corner states, which are distinct from traditional *in situ* type I corner states, exhibit different spatial locations and diverse phase profiles. The experimental validations using the kagome

lattice highlight the crucial role of long-range interactions in higher-order topological phases, providing alternative possibilities for precise control over acoustic waves. The agreement between the theoretical, simulation, and experimental results underscores the reliability of the findings. This work opens up avenues for various applications, including acoustic sensing, topological trapping, energy harvesting, and microparticle manipulation. In summary, this study expands the understanding of topological corner states in acoustic systems and their potential applications, paving the way for future advancements in acoustic wave control and design.

ACKNOWLEDGMENTS

We thank Z.-K. Lin of Soochow University for helpful discussions. This work was supported by the National Key R&D Program of China (Grants No. 2022YFA1404500 and No. 2022YFA1404400), the NSFC (Grants No. 12074183, No. 11834008, No. 12104226, No. 12227809, and No. 12225408), and the Fundamental Research Funds for the Central Universities (Grants No. 020414380181 and No. 020414380211). Z.Z. acknowledges support from the Funds for Zijin Scholars of Nanjing University.

[1] M. Z. Hasan and C. L. Kane, Colloquium: Topological insulators, Rev. Mod. Phys. **82**, 3045 (2010).
[2] X.-L. Qi and S.-C. Zhang, Topological insulators and superconductors, Rev. Mod. Phys. **83**, 1057 (2011).
[3] W. A. Benalcazar, B. A. Bernevig, and T. L. Hughes, Quantized electric multipole insulators, Science **357**, 61 (2017).
[4] W. A. Benalcazar, B. A. Bernevig, and T. L. Hughes, Electric multipole moments, topological multipole moment pumping, and chiral hinge states in crystalline insulators, Phys. Rev. B **96**, 245115 (2017).
[5] Z. Song, Z. Fang, and C. Fang, $(d-2)$-dimensional edge states of rotation symmetry protected topological states, Phys. Rev. Lett. **119**, 246402 (2017).
[6] J. Langbehn, Y. Peng, L. Trifunovic, F. von Oppen, and P. W. Brouwer, Reflection-symmetric second-order topological insulators and superconductors, Phys. Rev. Lett. **119**, 246401 (2017).
[7] F. Schindler, A. M. Cook, M. G. Vergniory, Z. Wang, S. Parkin, B. A. Bernevig, and T. Neupert, Higher-order topological insulators., Sci. Adv. **4**, eaat0346 (2018).
[8] M. Ezawa, Higher-order topological insulators and semimetals on the breathing kagome and pyrochlore lattices, Phys. Rev. Lett. **120**, 026801 (2018).
[9] F. Liu and K. Wakabayashi, Novel topological phase with a zero Berry curvature, Phys. Rev. Lett. **118**, 076803 (2017).
[10] C. W. Peterson, W. A. Benalcazar, T. L. Hughes, and G. Bahl, A quantized microwave quadrupole insulator with topologically protected corner states, Nature (London) **555**, 346 (2018).
[11] Y. Ota, F. Liu, R. Katsumi, K. Watanabe, K. Wakabayashi, Y. Arakawa, and S. Iwamoto, Photonic crystal nanocavity based on a topological corner state, Optica **6**, 786 (2019).
[12] X.-D. Chen, W.-M. Deng, F.-L. Shi, F.-L. Zhao, M. Chen, and J.-W. Dong, Direct observation of corner states in second-order topological photonic crystal slabs, Phys. Rev. Lett. **122**, 233902 (2019).
[13] M. Li, D. Zhirihin, M. Gorlach, X. Ni, D. Filonov, A. Slobozhanyuk, A. Alù, and A. B. Khanikaev, Higher-order topological states in photonic kagome crystals with long-range interactions, Nat. Photonics **14**, 89 (2020).
[14] B. Xie, G. Su, H.-F. Wang, F. Liu, L. Hu, S.-Y. Yu, P. Zhan, M.-H. Lu, Z. Wang, and Y.-F. Chen, Higher-order quantum spin Hall effect in a photonic crystal, Nat. Commun. **11**, 3768 (2020).
[15] H.-R. Kim, M.-S. Hwang, D. Smirnova, K.-Y. Jeong, Y. Kivshar, and H.-G. Park, Multipolar lasing modes from topological corner states, Nat. Commun. **11**, 5758 (2020).
[16] H.-X. Wang, L. Liang, B. Jiang, J. Hu, X. Lu, and J.-H. Jiang, Higher-order topological phases in tunable C_3 symmetric photonic crystals, Photonics Res. **9**, 1854 (2021).
[17] S. Imhof, C. Berger, F. Bayer, J. Brehm, L. W. Molenkamp, T. Kiessling, F. Schindler, C. H. Lee, M. Greiter, T. Neupert, R. Thomale, Topolectrical-circuit realization of topological corner modes, Nat. Phys. **14**, 925 (2018).
[18] M. Serra-Garcia, R. Süsstrunk, and S. D. Huber, Observation of quadrupole transitions and edge mode topology in an LC circuit network, Phys. Rev. B **99**, 020304(R) (2019).
[19] J. Bao, D. Zou, W. Zhang, W. He, H. Sun, and X. Zhang, Topoelectrical circuit octupole insulator with topologically protected corner states, Phys. Rev. B **100**, 201406(R) (2019).
[20] M. Serra-Garcia, V. Peri, R. Süsstrunk, O. R. Bilal, T. Larsen, L. G. Villanueva, and S. D. Huber, Observation of a phononic quadrupole topological insulator, Nature (London) **555**, 342 (2018).
[21] H. Fan, B. Xia, L. Tong, S. Zheng, and D. Yu, Elastic higher-order topological insulator with topologically protected corner states, Phys. Rev. Lett. **122**, 204301 (2019).
[22] Q. Wu, H. Chen, X. Li, and G. Huang, In-plane second-order topologically protected states in elastic kagome lattices, Phys. Rev. Appl. **14**, 014084 (2020).
[23] M. Yan, X. Huang, L. Luo, J. Lu, W. Deng, and Z. Liu, Acoustic square-root topological states, Phys. Rev. B **102**, 180102(R) (2020).
[24] X. Ni, M. Weiner, A. Alù, and A. B. Khanikaev, Observation of higher-order topological acoustic states protected by generalized chiral symmetry, Nat. Mater. **18**, 113 (2019).
[25] H. Xue, Y. Yang, F. Gao, Y. Chong, and B. Zhang, Acoustic higher-order topological insulator on a kagome lattice, Nat. Mater. **18**, 108 (2019).
[26] X. Zhang, H.-X. Wang, Z.-K. Lin, Y. Tian, B. Xie, M.-H. Lu, Y.-F. Chen, and J.-H. Jiang, Second-order topology and multidimensional topological transitions in sonic crystals, Nat. Phys. **15**, 582 (2019).
[27] Z. Zhang, M. Rosendo López, Y. Cheng, X. Liu, and J. Christensen, Non-Hermitian sonic second-order topological insulator, Phys. Rev. Lett. **122**, 195501 (2019).
[28] Z. Zhang, H. Long, C. Liu, C. Shao, Y. Cheng, X. Liu, and J. Christensen, Deep-subwavelength holey acoustic

second-order topological insulators, Adv. Mater. **31**, 1904682 (2019).
[29] L.-Y. Zheng and J. Christensen, Dirac hierarchy in acoustic topological insulators, Phys. Rev. Lett. **127**, 156401 (2021).
[30] Y. Yang, J. Lu, M. Yan, X. Huang, W. Deng, and Z. Liu, Hybrid-order topological insulators in a phononic crystal, Phys. Rev. Lett. **126**, 156801 (2021).
[31] L. Ye, C. Qiu, M. Xiao, T. Li, J. Du, M. Ke, and Z. Liu, Topological dislocation modes in three-dimensional acoustic topological insulators, Nat. Commun. **13**, 508 (2022).
[32] D. Liao, Z. Zhang, Y. Cheng, and X. Liu, Engineering negative coupling and corner modes in a three-dimensional acoustic topological network, Phys. Rev. B **105**, 184108 (2022).
[33] X. Huang, J. Lu, Z. Yan, M. Yan, W. Deng, G. Chen, and Z. Liu, Acoustic higher-order topology derived from first-order with built-in Zeeman-like fields, Sci. Bull. **67**, 488 (2022).
[34] H. Xue, Y. Yang, and B. Zhang, Topological acoustics, Nat. Rev. Mater. **7**, 974 (2022).
[35] Q. Wei, X. Zhang, W. Deng, J. Lu, X. Huang, M. Yan, G. Chen, Z. Liu, and S. Jia, Higher-order topological semimetal in acoustic crystals, Nat. Mater. **20**, 812 (2021).
[36] L. Luo, H.-X. Wang, Z.-K. Lin, B. Jiang, Y. Wu, F. Li, and J.-H. Jiang, Observation of a phononic higher-order Weyl semimetal, Nat. Mater. **20**, 794 (2021).
[37] H. Qiu, M. Xiao, F. Zhang, and C. Qiu, Higher-order Dirac sonic crystals, Phys. Rev. Lett. **127**, 146601 (2021).
[38] W. Zhu, H. Xue, J. Gong, Y. Chong, and B. Zhang, Time-periodic corner states from Floquet higher-order topology, Nat. Commun. **13**, 11 (2022).
[39] H. Liu, X. Huang, M. Yan, J. Lu, W. Deng, and Z. Liu, Acoustic topological metamaterials of large winding number, Phys. Rev. Appl. **19**, 054028 (2023).
[40] Z. Deng, X. Zhang, D. Gao, M.-H. Lu, and X. Zhang, Deterministic generation of multiple topological corner states based on an extremely expanded coupling condition, Phys. Rev. Res. **4**, 033084 (2022).
[41] H. Yang, L. Song, Y. Cao, and P. Yan, Observation of type-III corner states induced by long-range interactions, Phys. Rev. B **106**, 075427 (2022).
[42] See Supplemental Material at http://link.aps.org/supplemental/10.1103/PhysRevB.109.024305 for details about the origin and limitation of type-N corner states, the tight-binding model of the SSH lattice with next-nearest-neighbor coupling, type II and type III corner states of the acoustic SSH lattice, Wannier representations of the 2D SSH model with NNN coupling, details of the acoustic kagome lattice and the SSH lattice, the effects of breaking C_3 symmetry on corner-localized states, and numerical and experimental methods. The Supplemental Material also contains Refs. [43,44].
[43] Z.-K. Lin, Y. Wu, B. Jiang, Y. Liu, S.-Q. Wu, F. Li, and J.-H. Jiang, Topological Wannier cycles induced by sub-unit-cell artificial gauge flux in a sonic crystal, Nat. Mater. **21**, 430 (2022).
[44] B. Bradlyn, L. Elcoro, J. Cano, M. G. Vergniory, Z. Wang, C. Felser, M. I. Aroyo, and B. A. Bernevig, Topological quantum chemistry, Nature (London) **547**, 298 (2017).
[45] X. Cai, L. Ye, C. Qiu, M. Xiao, R. Yu, M. Ke, and Z. Liu, Symmetry-enforced three-dimensional Dirac phononic crystals, Light Sci. Appl. **9**, 38 (2020).
[46] Z.-G. Chen, L. Wang, G. Zhang, and G. Ma, Chiral symmetry breaking of tight-binding models in coupled acoustic-cavity systems, Phys. Rev. Appl. **14**, 024023 (2020).
[47] Y. Deng, W. A. Benalcazar, Z.-G. Chen, M. Oudich, G. Ma, and Y. Jing, Observation of degenerate zero-energy topological states at disclinations in an acoustic lattice, Phys. Rev. Lett. **128**, 174301 (2022).
[48] H.-X. Wang, G.-Y. Guo, and J.-H. Jiang, Band topology in classical waves: Wilson-loop approach to topological numbers and fragile topology, New J. Phys. **21**, 093029 (2019).
[49] D. Liao, Y. Liu, Z. Zhang, Y. Cheng, X. Liu, and J. Christensen, Synthesizing topological acoustic rainbow trapping at deep-subwavelength corners, Sci. Bull. **68**, 1744 (2023).
[50] C. Liu, Z. Zhang, D. Liao, Z. Yue, C. Ma, Y. Cheng, and X. Liu, Rainbow trapping for sound waves in one-dimensional topological insulator, Appl. Phys. Lett. **123**, 041701 (2023).